Direct Observation of Heterogeneous Surface Reactivity and Reconstruction on Terminations of Grain Boundaries of Platinum

Xiao Zhao,[1]* Takao Gunji,[1] Fan Lv,[2] Bolong Huang,[3]* Rui Ding,[4] Jianguo Liu,[4]* Mingchuan Luo,[2] Zhigang Zou,[4] Shaojun Guo[2]*

[1]Innovation Research Center for Fuel Cells, The University of Electro-Communications, Chofugaoka, Chofu, Tokyo 182-8585, Japan.

[2]Department of Materials Science and Engineering, and BIC-ESAT, College of Engineering, Peking University, Beijing 100871, China.

[3]Department of Applied Biology and Chemical Technology, The Hong Kong Polytechnic University, Hung Hom, Kowloon, Hong Kong SAR.

[4] Jiangsu Key Laboratory for Nano Technology, National Laboratory of Solid State Microstructures, College of Engineering and Applied Sciences, and Collaborative Innovation Center of Advanced Micro-structures, Nanjing University, 22 Hankou Road, Nanjing 210093, China.

*Correspondence to: xiaozhao@uec.ac.jp (X.Z.); bhuang@polyu.edu.hk (B.H.); jianguoliu@nju.edu.cn (J.L.); guosj@pku.edu.cn (S. G.)

Abstract: Direct observation of the reactivity of atomically resolved defects has always been desired in catalysis study, but never realized experimentally. Here, we report the first experimental "recordation" and "storage" of catalytic trajectories *via* environmental transmission electron microscopy, and further collectively reveal the reactivity profiles on atomically resolved defects without compromising the spatial resolution. A defect surface-catalyzed graphitic layer growth model reaction was used as the probe to demonstrate the reactivity of different defects, which finally allows us to directly establish a coordination-strain-reactivity-surface restructuring correlation. Our results reveal that (1) the reactivity of strained stepped facets is much higher than that of close-packed facets, and increases with local strains/energetics, and (2) during the thermal growth of graphitic overlayers on platinum defective surfaces, the surface restructurings were mainly determined by two competing

processes: thermal-induced surface smoothening and adsorbates-induced surface low-coordinating processes, making the reactivity self-decayed and self-enhanced, respectively. DFT calculations reveal a novel rhombohedral Volcano-type Zebra-crossing plot for the structure-activity relation regarding the improved reactivity by strained defect sites, totally different from a conventional Volcano-type plot in catalysis studies. Our findings demonstrate an ideal technique for the direct and explicit identification of atomically-resolved catalytically-active defects that may display revolutionary influence in the future catalysis explorations.

One Sentence Summary: Watch a catalytic reaction occurring where and how fast on the atomically resolved surface

Main Text: Heterogeneous catalysis plays a central role in modern chemical and energy industries. Searching the optimal active sites has always been a "holy grail" in catalysis. The catalytically active sites are often unsaturated, proposed by Taylor in 1925 (*1*). Experimentally, active sites usually appear low-coordinated (*1-4*) or strained (*5-7*). Generally, a nanocatalyst contains one or more types of defects including vacancies, atomic steps, dislocations, grain boundaries (GBs) and lattice faults. Among them, the GBs—an inherent structural component in polycrystalline materials—play a crucial role in determining the performance of nanocatalysts (*8-12*), structural materials (*13, 14*) and energy materials (*15, 16*)—a function of materials gene. However, the GBs usually arise with other defects such as atomic steps, dislocations and local strains (*8-12*). Moreover, these multiple *yet* rather diverse defects change dynamically with *in-situ* restructurings that frequently occur in reactive environments (*17-19*) or catalytic processes (*2, 20, 21*). Therefore, the synchronous determination of defects with their reactivity is, thus, necessary but still a great challenge. Recent advances in *in-situ* techniques have realized the direct observation of surface structures and their reactivity at the nanoscale or atomic scale (*2, 3, 22-27*). However, the practical spatial resolutions in *in-situ* scanning tunneling microscopy (STM) and environmental transmission electron microscopy (ETEM) have been suffered from remarkable reduction due to the dynamic interferences from the adsorption of reactants and the desorption of products, resulting in the loss of partial structure-reactivity information (*2, 3, 25, 26*).

Herein, we first document the *in-time* catalytic trajectories and corporately present reactivity profiles on different defects without sacrificing the spatial resolution through environmental

transmission electron microscopy. Excitingly, we achieve a direct observation of the reactivity of atomically resolved defects. The Pt nanorods assembly (NRA) with different defects (Fig. S1) was used as a model catalyst to catalyze the graphitic layer growth over the defects. We identified a new coordination-strain-reactivity-surface restructuring correlation for a surface-catalyzed graphitic layer growth model reaction on individual Pt NRA, in which (1) the reactivity on strained stepped facets increases with local strains/energetics, and is much higher than that on close-packed facets, and (2) the thermal induced surface smoothening and adsorbates induced surface low coordinating processes competitively control surface restructurings, and make the reactivity self-decayed and self-enhanced, respectively. DFT calculations revealed the superior reactivity on strained defect sites that follow a rhombohedral Volcano-type Zebra-crossing plot, instead of the conventional Volcano-type plot. Our new finding greatly resolves the problem that studying atomically-resolved fully-detailed GBs has always been obstructed by the randomly-oriented and high-angle grains (see the example in Fig. S2) (*8-13, 15, 16, 28*).

Fig. 1

As shown in Fig. 1, the GBs, as a type of planar defects, appear with other defects. Low-coordinated atomic steps form the strained stepped facets with low-index terraces on the concave terminations of GBs (Fig. 1A). The misorientated angle was estimated to be *ca.* 0.6° through comparing fast Fourier transform patterns between Grain-1 and Grain-2 (Fig. 1B). A few of point defect (*e.g.* atomic vacancies) arise around the centre regions of GBs (Fig. 1C). Edge dislocations emerge with GBs and stabilize the misorientated grains geometrically. The geometric compatibility, wherein surface atoms must accommodate each other, makes edge dislocations diffuse toward adjacent grains and form dislocations-induced strain arrays. A strain gradient field, thus, forms by surrounding the core of edge dislocation (*8*). Anisotropic GBs complicate the atom arrangements, for examples, the appearance of local distortion on the surface of Gain-2 that is connected simultaneously with Grains-1,3,4 (Fig. 1C and see more examples in Fig. S2). An analysis of d(200) spacing (Fig. 1D) shows the regions adjacent GBs appear compressive (1.86-1.91 *vs.* bulk 1.96 Å), while the regions far from GBs are relaxed (d(200)=2.02 Å) to relieve compressive strains. Overall, the structural analysis of GBs (see an atomic model of GB in Fig. 1E) suggests that not only defect themselves but also their influences on neighboring atoms should be included to understand the defect effect. These multiple *yet*

rather diverse defects naturally raise the challenge for the accurate understanding and thus finding of catalytically active defects.

Fig. 2

Figure 2A-C sketches our basic idea to address this fundamental challenge by developing an *in-situ* solid-phase probing reaction (a defect surface-catalyzed graphitic layer growth model reaction). We investigated a single Pt NRA that is supported on a carbon microcoil (CMC, Fig. S1). Under the thermal and vacuum conditions, carbon atoms in CMC were activated, subsequently, migrate and grow in the form of graphitic overlayers on surfaces of Pt NRA, similar to the phenomenon reported by Tauster *et al.* in 1978, and caused by strong metal-support interactions (*29, 30*). The number of graphic overlayers is determined by and thus correlated with the reactivity of platinum nanofacets. This probing process likes "drawing" reactivity profiles on catalytic surfaces using the product of graphitic overlayers as the solid "pigment". Through utilizing ETEM, we directly observe where and how fast a reaction occurs on atomically resolved defective surfaces, to our best knowledge, which is the firstly reported to date (*2, 3, 19, 23-27, 31, 32*) (see the summary in Table S1 on the key abilities for different *in-situ* techniques).

Figure 2D shows the initial state of a Pt NRA that has similar structures with the one in Fig. 1 (see the structural analysis in Fig. S3). After the thermal treatment at 300 °C for 30 min (GB-300), graphitic overlayers appeared on the surfaces of GB-300 (Fig. 3E), and were seen distinctly from the initial state (Fig. 2D), accompanied with the *in situ* restructuring of Pt nanofacets. Notably, during the thermal reaction, the electron beam was turned off to avoid possible interferences for Pt nanofacets and/or the growth of graphitic overlayers. Clearly, the distribution of graphitic overlayers on Pt nanofacets is not uniform but structure-sensitive with the trend: the concave terminations on high-angle GB (D1) > the concave terminations on low-angle GB (D4) > the domains on twin boundaries (D2, D6) > the regions on convex parts (D3, D5) (Fig. 2F, see more details in Fig. S4-S9). According to the abovementioned structural analysis, this trend in catalytic reactivity is correlated simultaneously with the coordination numbers and strains of surface sites.

Specifically, an evidently higher reactivity on the stepped surfaces (Surfaces 5-9) was observed than that on the close-packed surfaces (Surface-2, 4, 10, 11) (*2, 25, 33-35*). The enhanced reactivity on the stepped surfaces corresponds to their up-shifted d-states (*34, 35*). However, the reactivity on the

stepped surfaces is not the same that varies remarkably with local strains/energetics, which is a firstly direct observation of such a phenomenon. For instance, the numbers of graphitic overlayers on Surfaces-6, 7, 8, which locate at the concave center, increase by a factor of 1-2 than that on Surface-5, 9, which are far from the concave centre. This trend in strain-dependent reactivity also happened for the regions: the high-angle GB > the low-angle GB > the twin boundaries > the close-packed surfaces. Overall, the reactivity on the stepped surfaces increases with local strains, thereby suggesting the direction for the design of high-performance nanocatalysts. On the other hand, the surface restructurings occurred, and their degrees increase with local strains. For example, the more remarkable restructuring occurred on the concave terminations of low-angle GB (D4) than on the twin boundary (D2). However, the consequences for the surface restructurings are not always the same because both microroughened (D2, D4) and smoothened (D5) surfaces are observable.

Interestingly, carbon-trapped adatoms and even single atoms of Pt are noticed and marked by the red and yellow circles, respectively (see more details in Fig. S4-S15). The structural restructuring toward low-coordinated steps, adatoms and single atoms (briefly denoted as the low-coordinating process) agrees with the reports on the atomization of Pt, Au, and Pd from their NPs (*33, 36*) as well as the formations of Ni adatoms (*26*) and Pt, Ru and Au steps from their bulk surfaces (*2, 18, 37, 38*) in reactive environments. Thus, this low-coordinating process should be quite general and often accompanied by the enhanced reactivity (*1, 2*). The driving force is that the binding energy of low-coordinated atoms to adsorbates exceeds that of bulk counterparts (*33, 36, 38*). That adatoms and single atoms of Pt are observable after a thermal reaction, indicating that they are kinetically stable.

Fig. 3

To acquire in-depth insights into the surface restructurings and the associated responses for the reactivity, we further treated GB-300 at 500 °C for 15 min under the vacuum condition (denoted as GB-300-500). As shown in Fig. 3, the GB-300-500 presents three remarkable changes. (i) The concave terminations of high-angle GB (D1) became smoothened and concurrently the number of graphitic overlayers decreased by a factor of 2-4. (ii) The microroughening degree at the twin region (D2) increased and concurrently the number of graphitic overlayers increased by a factor of 1. (iii) The microroughening degree at the low-angle GB (D4) increased, and the number of graphitic overlayers increases by a factor of 1. These changes in surface structures and associated reactivity suggest: (i)

again, the strained stepped surfaces are more reactive than the close-packed surfaces; (ii) the microroughened surfaces gave rise to a self-enhanced reactivity at the D2 and D4 regions; (iii) the smoothened surface at the D1 region experienced a decreased reactivity. Accompanied by the surface restructurings and the influenced reactivity, the surface migration of reaction intermediates may occur from D1 and D5 to D2 and D4, respectively. Meanwhile, after performing a reaction at 500 °C, the maintenance of strained stepped surfaces at the D2 and D4 regions verifies their metastable state presumably due to the change in surface energies induced by graphitic overlayers (*19*).

The interesting question is, under the same reaction condition, why the domain at the high-angle GB (D1) became smooth while the regions at the twin (D2) and low-angle GB (D4) became rough. Depending on the misorientation angles, the energetics of GBs follow the trend: the high-angle GBs >> the ultralow-angle GBs > the twin boundary (*14*). To release the significantly excessive energy, the restructuring for the domains at the high-angle GBs (D1) was, thus, dominated by the thermal-induced surface smoothening process. In contrast, for the regions at the twin (D2) and the ultralow-angle GBs (D4, the misorientation angle is 0.7°), the restructurings were mainly controlled by the adsorbates-induced surface low-coordinating process. The consequences of surface restructuring are therefore mainly determined by the two competing processes—the thermal-induced surface smoothening and the adsorbates-induced surface unsaturated processes in reactive environments. Carbon-trapped Pt adatoms and single atoms are still observable in the GB-300-500, demonstrating their kinetic stability again (*33, 36, 38*).

Fig. 4

For the further insight of the surface structural evolution, we explored the electronic structures of GB models with distinct atom arrangements and strains by DFT calculations. To accurately compare the electronic activities, we considered the dominant peak of Pt-5d band (d-pk), which directly determines the 5d electronic exchange and transfer (5d-EXT) ability for (electro)catalysis. Meanwhile, another reactivity indicator, the total barrier for activating electron-transfer from the surface, has been compared *via* the sum of surface work-function (Φ) and the dominant peak position of Pt-5d band (d-pk). Taking the face-centered cubic (*fcc*)-Pt-bulk metal as the reference, currently studied GB surfaces are meta-stable if introducing structural strains, thereby suggesting a suitable strain is necessary to balance the activity and stability.

The calculation results highlight a rhombohedral Volcano-type Zebra-crossing (RVZ) region wherein the GB model surfaces possess the shallowest depths of d-pk values and the potentially highest 5d-EXT abilities (Fig. 4A). Within the same energetic range, the GB models in RVZ region display the minimum electron-transfer barriers for electrocatalysis, as indicated by the inversed RVZ-plot (Fig. 4B). To estimate the strain effects on 5d-EXT, the elastic strain moduli of nano-surfaces were introduced using the Lamé parameters within the realm of simplified continuum mechanics. The electronic activities of model surfaces evidently increase with the enlarged strains, achieving the optimal electronic structures in the RVZ region (Fig. 4C). In contrast with pure (111) surface and *fcc* lattice, the projected partial density of states (PDOSs) of selected model surfaces from the RVZ region exhibit highly lying Pt-5d states near the Fermi level (E_F) as well as finely modulated peak positions for a tuned selectivity of electron transfer (Fig. 4D). Such electronic properties ensure both the activities and selectivity for catalysis. The real spatial contour plots for bonding and anti-bonding orbitals near the E_F indicate the electron-rich characters of the strained defective surfaces (Fig. 4E). Therefore, the optimal electronic activities for catalysts could be realized by introducing structural strains into the defective sites such as GB, atomic vacancies, step edges, interfaced edges and disordered surfaces, as indicated in the RVZ region, which is in agreement with the experimental results of higher reactivity of GB surfaces than the close packed surfaces. In line with *in-situ* ETME observations and DFT calculations, Pt NRA/CMC is also much more active than the commercial Pt/C catalyst for the oxygen reduction reaction (ORR), a vital reaction for the technologies of fuel cells and metal-air batteries (Fig. S16).

References and Notes:

1. H. S. Taylor, *Proceedings of the Royal Society of London. Series A* **108**, 105-111 (1925).
2. T. Zambelli, J. Wintterlin, J. Trost, G. Ertl, *Science* **273**, 1688-1690 (1996).
3. S. Helveg *et al.*, *Nature* **427**, 426-429 (2004).
4. R. van Lent *et al.*, *Science* **363**, 155-157 (2019).
5. P. Strasser *et al.*, *Nature Chem.* **2**, 454-460 (2010).
6. L. Wang *et al.*, *Science* **363**, 870-874 (2019).
7. M. Luo, S. Guo, *Nature Reviews Materials* **2**, 17059 (2017).
8. R. G. Mariano, K. McKelvey, H. S. White, M. W. Kanan, *Science* **358**, 1187-1192 (2017).
9. X. Huang *et al.*, *Nano Lett.* **14**, 3887-3894 (2014).
10. X. Feng, K. Jiang, S. Fan, M. W. Kanan, *J. Am. Chem. Soc.* **137**, 4606-4609 (2015).
11. Y. Wang, P. Han, X. Lv, L. Zhang, G. Zheng, *Joule*, 2551-2582 (2018).
12. X. Feng, K. Jiang, S. Fan, M. W. Kanan, *ACS Central Science* **2**, 169-174 (2016).
13. Z. Cheng, H. Zhou, Q. Lu, H. Gao, L. Lu, *Science* **362**, eaau1925 (2018).
14. K. Lu, *Nature Reviews Materials* **1**, 16019 (2016).
15. P. Yan *et al.*, *Nature Energy* **3**, 600-605 (2018).
16. D.-Y. Son *et al.*, *Nature Energy* **1**, 16081 (2016).
17. F. Tao *et al.*, *Science* **327**, 850-853 (2010).
18. Y. He *et al.*, *Proceedings of the National Academy of Sciences* **115**, 7700-7705 (2018).
19. P. L. Hansen *et al.*, *Science* **295**, 2053-2055 (2002).
20. F. Tao *et al.*, *Science* **322**, 932-934 (2008).
21. L. Cao *et al.*, *Nature Catalysis* **2**, 134–141 (2018).
22. W. L. Xu, J. S. Kong, Y. T. E. Yeh, P. Chen, *Nature Mater.* **7**, 992-996 (2008).
23. X. C. Zhou *et al.*, *Nat. Nanotechnol.* **7**, 237-241 (2012).
24. C.-Y. Wu *et al.*, *Nature* **541**, 511 (2017).
25. J. H. K. Pfisterer, Y. Liang, O. Schneider, A. S. Bandarenka, *Nature* **549**, 74-77 (2017).
26. L. L. Patera *et al.*, *Science* **359**, 1243-1246 (2018).
27. J. H. Zhong *et al.*, *Nat. Nanotechnol.* **12**, 132-136 (2017).
28. C. W. Li, J. Ciston, M. W. Kanan, *Nature* **508**, 504 (2014).
29. S. J. Tauster, S. C. Fung, *J. Catal.* **55**, 29-35 (1978).
30. S. J. Tauster, S. C. Fung, R. L. Garten, *J. Am. Chem. Soc.* **100**, 170-175 (1978).
31. T. Chen *et al.*, *Chem. Rev.* **117**, 7510-7537 (2017).
32. N. Zou *et al.*, *Nature Chem.* **10**, 607–614 (2018).
33. J. Jones *et al.*, *Science* **353**, 150-154 (2016).
34. J. K. Norskov *et al.*, *Chem. Soc. Rev.* **37**, 2163-2171 (2008).
35. B. Hammer, J. K. Norskov, *Nature* **376**, 238-240 (1995).
36. S. Wei *et al.*, *Nat. Nanotechnol.* **13**, 856-861 (2018).
37. F. Tao, M. Salmeron, *Science* **331**, 171-174 (2011).
38. P. Thostrup *et al.*, *Phys. Rev. Lett.* **87**, 126102 (2001).

Acknowledgement

Author contributions: X.Z., B.H., J.L. and S.G. conceived the project. X.Z. and T.G. conducted in-situ ETME experiments. X.Z. and F. L. prepared the Pt NRA/CMC catalyst. B.H. conducted DFT calculations. All authors revised and discussed the manuscript.

Competing interests: None declared.

Data and materials availability: The data presented in this paper are available in the supplementary materials

SUPPLEMENTARY MATERIALS: Materials and Methods

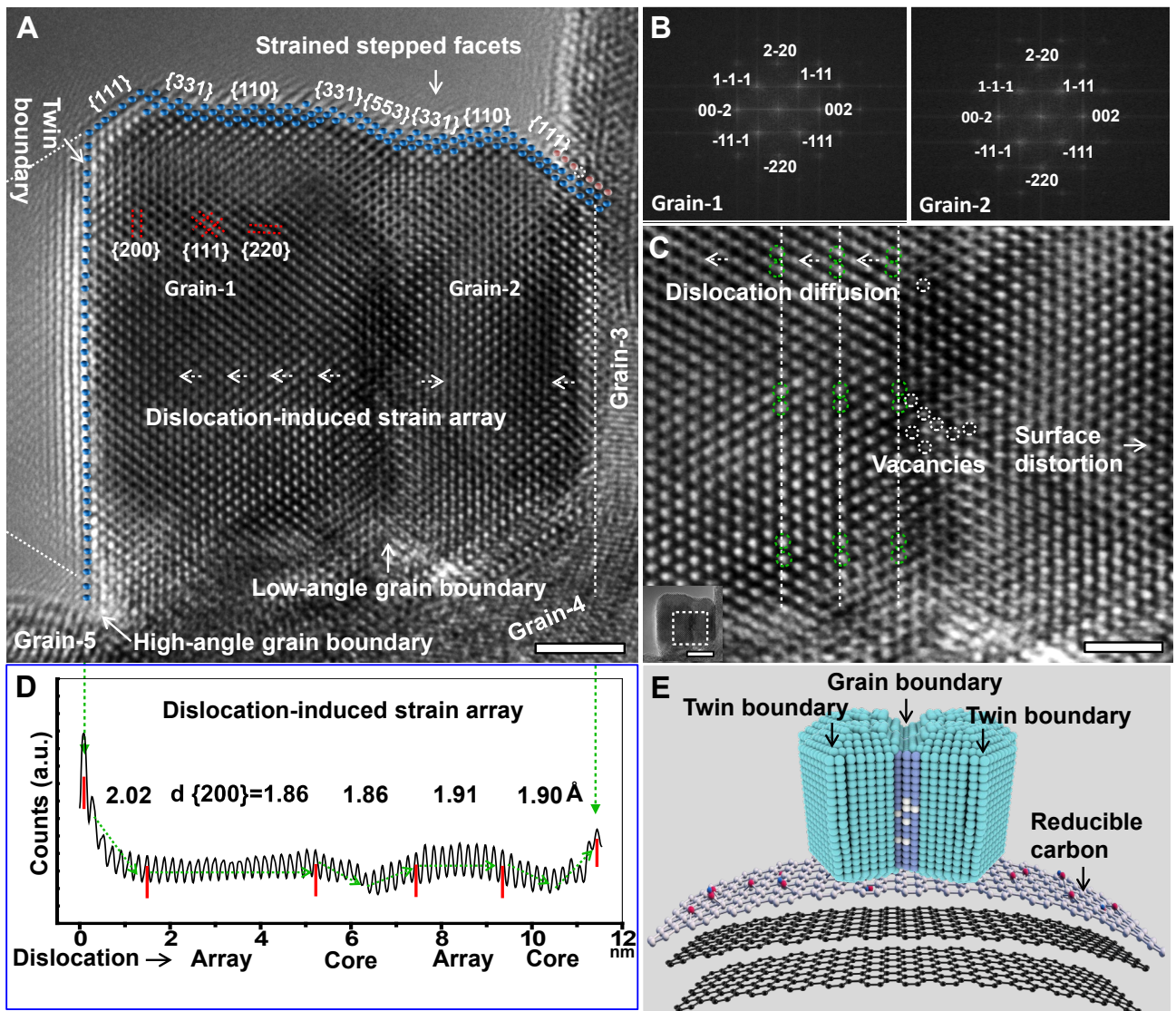Figs. S1 to S16

Tables S1

References (39-53)

Fig. 1. Atomically resolved structural analysis of a Pt NRA. (**A**) Atomically resolved ETEM image for a Pt NRA. (**B**) Fast Fourier transform (FFT) patterns for Grain-1 and Grain-2. (**C**) Dislocation diffusion analysis for the marked centre region in the *inset*; white cycles indicate atomic vacancies. (**D**) Analysis of a dislocation-induced strain array along the {200} orientation. (**E**) A atomic model for a Pt NRA nanoparticle supported on graphene planes. Scale bars in (**A**) and (**C**) are 2 and 1 nm, respectively.
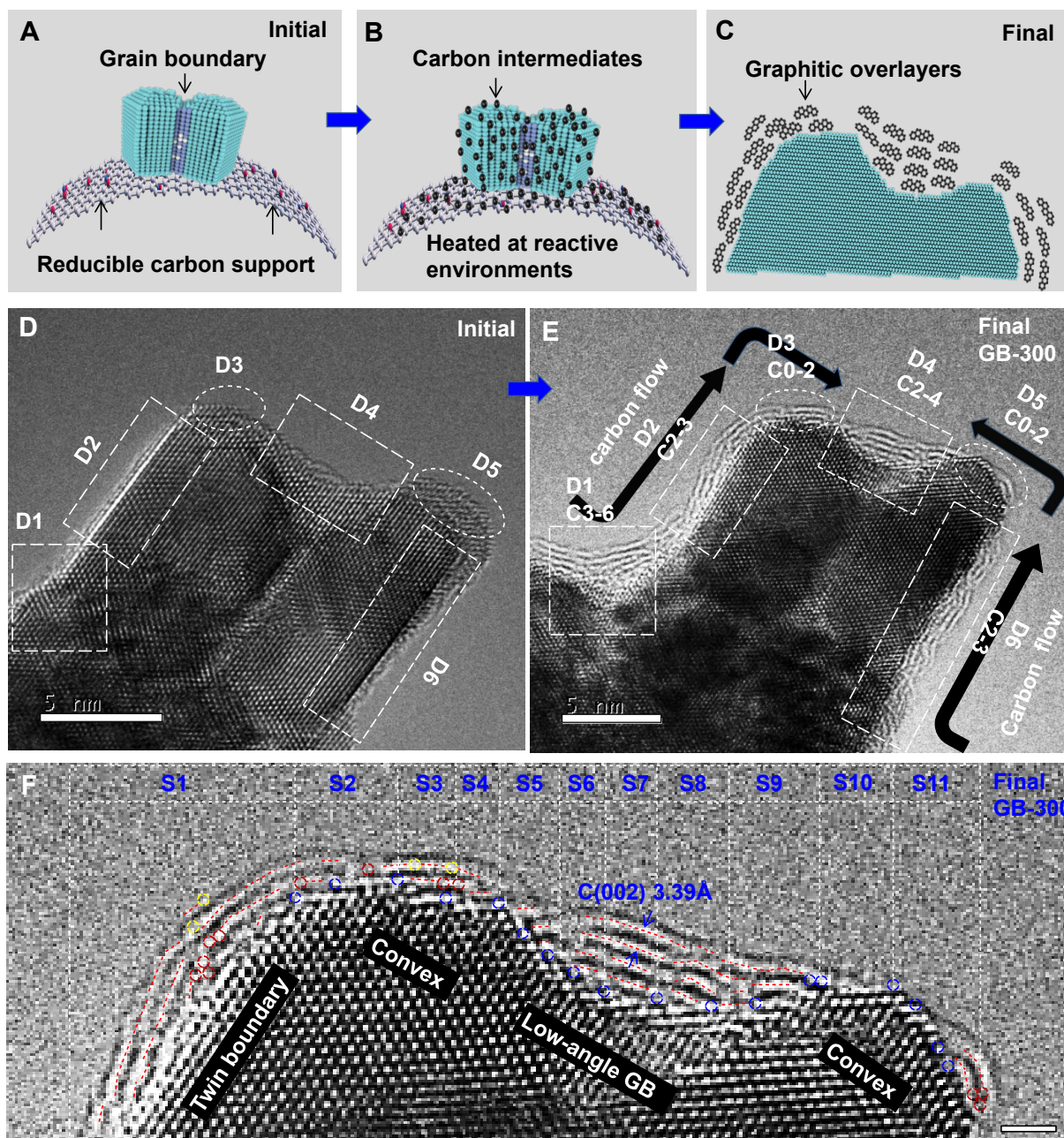
Fig. 2. Direct observation of the reactivity of atomically resolved defects. (**A** to **C**) A scheme for an *in situ* solid-phase probing reaction. (**D** to **E**) Atomically resolved ETEM images of a Pt NRA nanoparticle at the initial state (D) and after the reaction at 300 °C for 30 min (E). (**F**) Atomic scale correlation of surface sites with their catalytic reactivity. D-numbers represents the different surface domains; C-numbers denotes the number of graphitic overlayers on surface sites, which quantitatively characterizes the catalytic reactivity. Scale bars in (D, E, F) are 5, 5 and 1 nm, respectively. The red and yellow dotted line cycles indicate atomic steps (or adatoms or clusters) and single-atoms, respectively. The interplanar spacing of 3.39 Å corresponds to the lattice fringe of graphite (002). The red dotted lines indicate graphitic sheets.
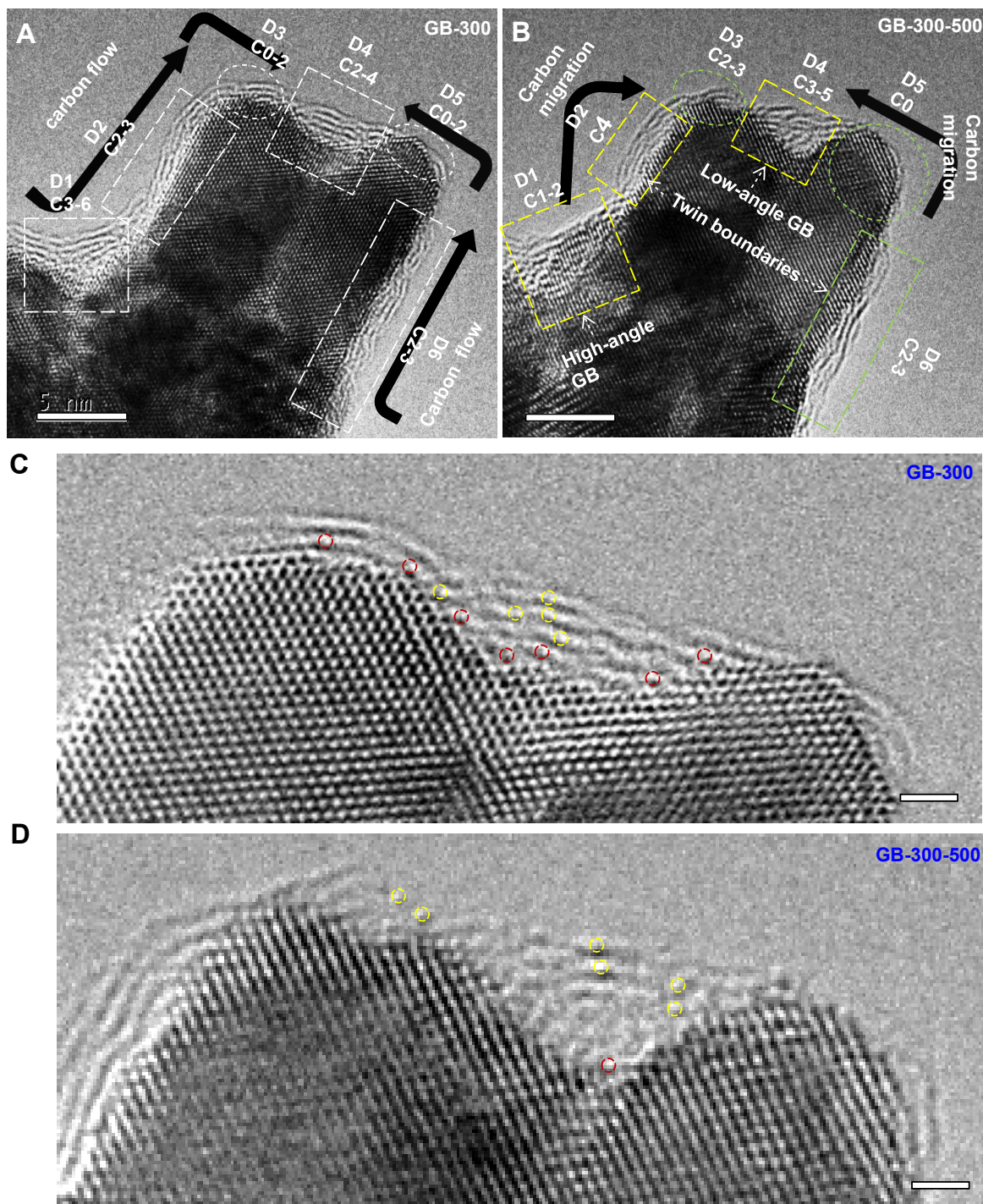
Fig. 3 Direct observation of *in situ* surface restructurings and the associated responses for the catalytic reactivity. (**A to D**) Atomically resolved ETEM images for GB-300 (A, C) and GB-300-500 (B, D). D-numbers represents different surface regions; C-numbers denotes the numbers of graphitic overlayers. Scale bars in (A, B) and (C, D) are 5 and 1 nm, respectively. The yellow dotted line rectangles in (B) highlight the regions with significant surface restructurings. The regions marked by the light green cycle and rectangle in (B) suggest the surfaces with the relatively weak surface structuring. ETEM images in (C, D) are focused on platinum surface structural details. The dark red and yellow dotted line cycles in (C, D) suggest platinum adatoms and platinum single atoms, respectively.
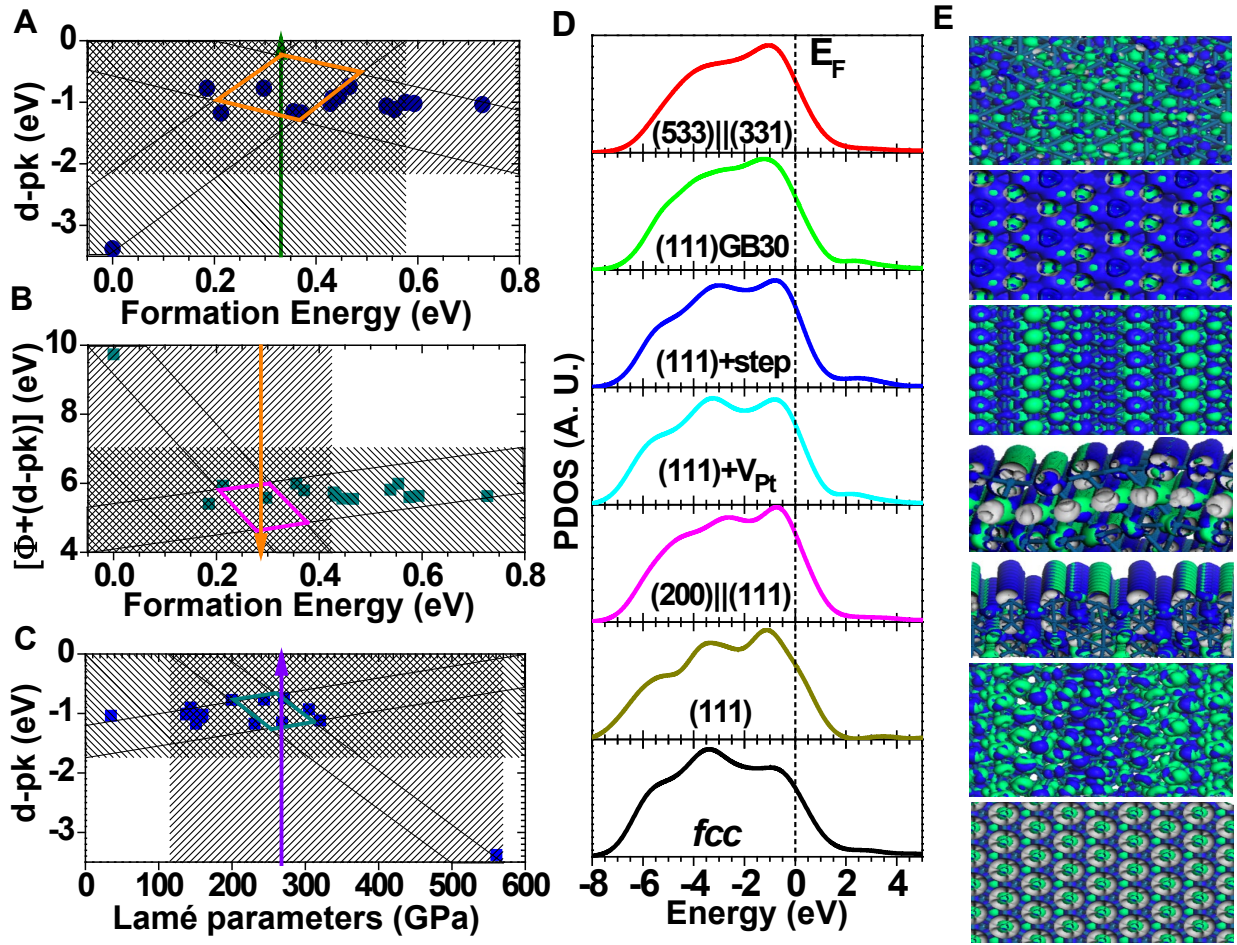
12

Fig. 4 Electronic structures and activities of Pt-surface models. (**A-C**) Energetic trends for the overall Pt-5d dominant peak positions (d-pk) (A) and total activation barriers [Φ+(d-pk)] with related to the normalized formation energies (*per fcc*-Pt-atom) (B) and Lamé parameters (C), respectively. (**D**) Projected partial density of states (PDOSs) of those electronically active Pt model surfaces selected from the RVZ-plot region (E_F denotes the Fermi level). The '*fcc*' and the 'GB30' denote the face-centered cubic and a grain boundary with a misorientation angle of 30°, respectively. (**E**) The real spatial contour plots for bonding and anti-bonding orbitals near E_F for the RVZ-plot selected models (bonding-orbital=blue isosurfaces; anti-bonding-orbital=green isosurfaces).